

Spectral Deconvolution Analysis of Mafic Mineral in Irregular Mare Patches on the Moon

Ik-Seon Hong¹, Yu Yi^{1†}, Nuri Park²¹Department of Astronomy, Space Science and Geology, Chungnam National University, Daejeon 34134, Korea²School of Earth and Space Exploration, Arizona State University, Tempe, AZ 85287, USA

Irregular mare patches (IMPs), recently discovered on the Moon, are eruptions of magma on the lunar surface, and their origins are still in question. While prior studies on IMPs have mainly focused on optical image analysis, in this study, an analysis of the characteristics of minerals is performed exemplary for the first time. Modified Gaussian model (MGM) deconvolution was applied to the infrared spectrum to confirm the properties of the mafic mineral. Mafic minerals were analyzed for 6 olivine-rich (Ol-rich) IMPs out of 91 currently reported, and only 4 of them yielded results of significance. All four sites showed more abundance of Fe than Mg, and manifested a weak relationship with Mg-suite rock. However, a problem was discovered during the MGM application process due to pilot implementation. In order to solve this problem, it is required to adjust the MGM initial condition settings more precisely and to increase the signal to noise ratio of the observation data. Moreover, it is necessary to analyze the mineral properties for all IMPs considering minerals other than Ol and utilize them to deduce the origin of the IMPs.

Keywords: Moon, irregular mare patches, mafic mineral, olivine, modified Gaussian model

1. INTRODUCTION

The distribution of minerals on the lunar surface provides a clue to how the Moon has evolved from the thermal and chemical standpoint. The Moon which we see today is the consequence of evolution as it went through the late heavy bombardment, magma oceans, differentiation of the mantle and crust, impacts, and volcanic activity. Much of the detailed mineral properties came to light when the Apollo program returned with lunar rock samples. Since there has been no plan to explore the Moon since the Apollo program until recently directly, studies on mineral property have been conducted mainly in the form of remote sensing, and as a result, mineral maps have been produced for the entire Moon (Nozette et al. 1994; McEwen et al. 1997; Lemelin et al. 2019; Lucey et al. 2000).

Lunar minerals are affected by various factors such as lunar evolution and space environment, etc. Thus, lunar

minerals can be studied from various perspectives. Lunar evolution, space weathering on the lunar surface, and volcanic activities such as magma eruptions, impacts, or melting are typical examples of them. Among those, lunar volcanic activity is the primary contributor to the formation of current lunar topography, and lava tubes, which are common in volcanic regions on Earth and have been discovered on Mars, have attracted attention among various terrains (Cushing et al. 2007; Cushing 2012; Hong et al. 2014; Jung et al. 2014, 2016).

Unlike the Earth, the Moon, which does not have a strong magnetic field and a thick atmosphere, is exposed to small-scale collisions by high-energy particles such as solar wind, cosmic rays, and micro meteorites introduced from external space. Hence, the physical and structural characteristics of the lunar regolith change gradually over time. This phenomenon is called space weathering. Direct observation of this phenomenon was made through analysis of samples

© This is an Open Access article distributed under the terms of the Creative Commons Attribution Non-Commercial License (<https://creativecommons.org/licenses/by-nc/3.0/>) which permits unrestricted non-commercial use, distribution, and reproduction in any medium, provided the original work is properly cited.

Received 28 NOV 2022 Revised 11 DEC 2022 Accepted 12 DEC 2022

[†]Corresponding Author

Tel: +82-42-821-5468, E-mail: euyiyu@cnu.ac.kr

ORCID: <https://orcid.org/0000-0001-9348-454X>

from the Apollo program (McCord & Johnson 1970; McCord & Adams 1973). The effect of space weathering on minerals can be identified through spectral lines of minerals. In the visible light region, reflectance decreases and looks darker, and in the near infrared region, the depths of the mineral absorption lines are becoming shallower and absorption lines shift to a longer wavelength (McCord & Adams 1973). It has been found that nanophase iron (np-Fe^0) in minerals is the cause of the variation in the spectral lines of minerals depending on space weathering (Pieters et al. 1993, 2000; Pieters & Noble 2016). From the spectral lines, which show space weathering over time, the relative age of various topography on the lunar surface can be estimated (Lucey et al. 1995, 2000; Grier et al. 2001; Yi et al. 2015; Sim et al. 2017; Sim & Kim 2018). In addition, solar wind particles are trapped in minerals to produce hydroxyl (OH), which could be a clue to the existence of lunar water (Kim et al. 2018).

It is known that the lunar topography can be largely divided into highlands and maria, with lunar maria mainly composed of basalt and highlands composed of anorthosite. The reason why the lunar maria looks dark is because of Fe and Mg, which constitute basalt, and minerals rich in these two elements are called mafic minerals. The lunar mafic minerals comprise olivine (Ol) and pyroxene primarily. Ol are known to originate from the mantle and are sometimes referred to as ultramafic because of their very high iron content (Wieczorek et al. 2006; Melosh et al. 2017). In order to understand the evolution of the Moon from the past, studies on the mantle as well as the lunar surface must be conducted. However, humans cannot reach the depth of the mantle directly in the Earth up until now, not to mention the Moon. Therefore, Ol that exist on the surface of the Moon can be said to be a clue that has information about the mantle, which is difficult for humans to reach directly. Hence, Ol are essential minerals for understanding the evolution of the Moon. However, care should be taken as Ol may not necessarily be originated from the mantle but may be a plutonic rock created by magma intruding into the lunar crust (Yamamoto et al. 2010).

Lunar Ol is a solid solution of Fe and Mg. While Fe-rich Ol are called fayalite ($\text{Fa, Fe}_2\text{SiO}_4$), Mg-rich Ol are called forsterite ($\text{Fo, Mg}_2\text{SiO}_4$) (BVSP 1981). The current mainstream explanation for the lunar evolution is as follows (Ringwood & Kesson 1976; Hess & Parmentier 1995; Elardo et al. 2011; Charlier et al. 2018; Li et al. 2019b). As the lunar magma ocean cools down and differentiates, the dense mafic minerals are crystallized first, forming Ol which sink into the lower mantle. After that, as pyroxene crystallizes, it takes the metals contained in magma, and plagioclase (Pl) of low density crystallizes on the lunar surface. Crystallized Pl form

the crust and become the current lunar highlands, while Ol and pyroxenes continue to crystallize and sink down. When entering the final stage of magma crystallization, the lunar crust composed of Pl gradually thickens, and ilmenite (Ilm, FeTiO_3) crystallize just below the crust. However, Ilms are denser than Ol sunk down already, creating a gravitational instability in the magma, and eventually, overturn of a positional reversal between the high-density minerals in the lower crust and Ol in the lower mantle occurs. Mg-rich Ol among the Ol after the overturn are located in the lower crust and are called Mg-suite rock (or Mg-suite magma). These are rarely found over the lunar surface. Also, volcanic activity such as magma eruption appears on the lunar surface due to the movement of magma. At the end of magma crystallization, potassium (K), rare earth elements (REE), and phosphorus (P) which are abundant in residual magma, crystallize in the lower crust to create the KREEP layer and stay at the same level as the Mg-suite rock.

Irregular mare patch (IMP) is a recently discovered terrain and has been explored with the distribution of high-resolution images of the Lunar Reconnaissance Orbiter Camera Narrow Angle Camera (LROC NAC) due to its small spatial scale. Ina, as shown in Fig. 1, is the first IMP discovered and is located at $18.66^\circ\text{N}, 5.3^\circ\text{E}$ the Lacus Felicitatis (Lake of Happiness). It was discovered in the images taken by Apollo 15 in 1971 due to its big size unlike other IMPs (Whitaker 1972). Based on the observation data at the time, Strain & El-Baz (1980) proposed that Ina was a topography created by magma erupted from the fissure. After high-resolution imaging became available, Garry et al. (2012) speculated that it was created by the expansion of lava flow, as there was no eruption spot of magma such as a crack in Ina.

Braden et al. (2014) searched for IMPs all over the Moon and found 70 of them, and updated location information of 91 IMPs is being distributed by NASA Planetary Data System (PDS) currently. 3 out of the 70 IMPs are estimated to be less than 100 million years old, and it is believed that after the volcanic activity completely stopped, these were created by small magma eruptions. Wilson & Head (2017) proposed a magmatic foam model to explain the IMP formation process. In this model, even after the surface of erupted magma is hardened, the active underlying magma below the surface is extruded through fissures on the hardened surface to form IMPs. According to this model, it is believed that most of the IMPs were created billions of years ago. Qiao et al. (2020) claimed that most IMPs were created in lunar maria that formed 3 billion years ago, coinciding with the peak of lunar volcanic activity. Byron et al. (2022) analyzed the thermal characteristics of the 8 largest IMPs and found that, unlike the general lunar maria, the thermal

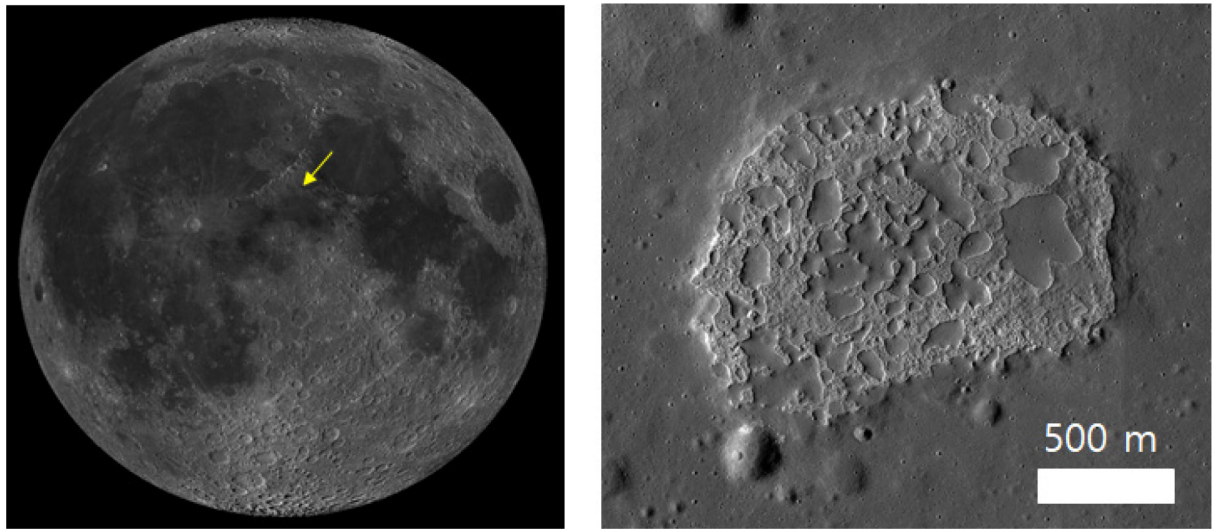


Fig. 1. Ina's location and appearance. It has a very different shape from the terrain normally seen on the Moon, with a small highland terrain between the surrounding mare and several small hills formed by the eruption of magma. The images were taken by the Lunar Reconnaissance Orbiter Camera Narrow Angle Camera (LROC NAC).

inertia was low. For the reason of this, they speculated that the materials comprising IMPs include small rocks weaker in strength than the general lunar regolith.

Since the IMP is a recently discovered terrain, there is not much research on it, and the origin of the IMP is being disputed by various studies. Previous studies have mainly analyzed optical images to derive scientific results, and no results of spectroscopic image analysis that can confirm mineral properties have been published yet. Therefore, in this study, deconvolution of spectral images is applied to areas of IMPs where olivine, a mafic mineral, is abundant to analyze mineral characteristics.

2. DATA AND METHOD

2.1 Data

The spectral characteristics of minerals appear mainly in the range of infrared (IR), and IR wavelengths have been observed by spectrometers mounted on orbiters whose main mission is to observe minerals in planetary or lunar exploration (Bibring et al. 2006; Pelkey et al. 2007; Ohtake et al. 2008; Green et al. 2011; Chen et al. 2020). The data used in this study are the spectral observation data of the Moon mineralogy mapper (M3) built by Brown University in USA, which was mounted on the Indian Space Research Organisation (ISRO) Chandrayaan-1 (Green et al. 2011).

The spectral observation data are presented in the form of a three-dimensional array consisting of two-dimensional images for each wavelength range. The observed wavelength

range is 446–3,000 nm, and the global mode data used for the analysis has a spectral resolution of 20–40 nm per each band, that is, 20 nm for short wavelength range and 40 nm for long wavelength range. There are total of 86 wavelength regions in a hyper-spectral type. While the spatial resolution is up to 140 m per pixel, but in actual data, it is about 200 m per pixel since the orbital altitude of Chandrayaan-1 was elevated due to an operation issue (Green et al. 2011). The data is distributed by NASA PDS and consists of raw data, radiance, and reflectance divided by three data processing steps, and in this analysis, reflectance data are used. Since the document of distributed reflectance data mentions the ground truth correction which was not applied to the data (Isaacson et al. 2013). Thus, we performed a ground truth correction.

The wavelength range used for this analysis is limited to 550–2,600 nm. The data in the short wavelength region are distributed hidden in the reflectance data, because it is not worth using for analysis since it does not contain any meaningful values in the image. Clark et al. (2011) and Li & Milliken (2016) pointed out that the spectral lines may be deformed in the wavelength region around 3,000 nm because the effect of heat remains even after thermal correction is performed. In addition, the analysis method to be applied is based on the mineral spectral library generated in the laboratory, and the wavelength range of the spectral data in the list is up to 2,600 nm.

2.2 Method

Spectral data deconvolution uses a modified Gaussian model (MGM). MGM is proposed by Sunshine et al. (1990)

and it is a technique to decompose spectral lines into Gaussian curves according to the initial conditions set by the user, and each Gaussian curve represents the characteristics of the mineral. Calculation code uses the one distributed by Brown University's NASA reflectance experiment laboratory (RELAB).

Ol shows a change in the shape of spectral lines depending on the composition ratio of Fe and Mg ($Fo\# = [(Mg^{2+} / (Fe^{2+} + Mg^{2+})) \times 100]$) and has a characteristic that the center of the largest absorption line shifts as a shorter wavelength (King & Ridley 1987). Sunshine & Pieters (1998) decomposed the absorption lines around 1,000 nm into three Gaussian curves while applying MGM to Ol, and showed that Relative Fo# could be determined from the trend of variation in the central wavelength of each Gaussian. Isaacson & Pieters (2010) showed that analysis could be made for Ol by decomposing absorption lines into three Gaussian curves using lunar rock samples. Isaacson et al. (2011) presented an effective continuum removal method for spectral lines with added continuum due to thermal effects while applying MGM to four Ol-rich regions with M3 spectral data. China's Chang'e-4 mission's Yutu rover is equipped with an IR spectrometer, which landed on the von Karman crater on the far side of the Moon. By applying MGM to the Ol data obtained by direct observation which has a higher signal to noise ratio (SNR) compared to remote sensing such as M3, it was revealed that the Ol in the landing area was of mantle origin (Li et al. 2019a; Gou et al. 2020).

Minerals on the lunar surface are unlikely to exist as a single mineral of Ol, and are likely to be present as a combination of various minerals. Therefore, when applying MGM to the mineral spectral lines, other minerals must be taken into account, and representative examples are pyroxene and Pl. Depending on the content of Ca, lunar pyroxene is classified into orthopyroxene (Opx) with low Ca and clinopyroxene (Cpx) with high Ca. Pyroxene with low Ca content is composed of Fe and Mg. Sunshine & Pieters (1993) showed that by applying MGM to pyroxene, the relative composition ratio of Opx and Cpx can be obtained with the depth of the Gaussian curve. Denevi et al. (2007) confirmed the relative composition ratio of Ca and Fe in pyroxene using the central wavelength of the Gaussian curve. Kanner et al. (2007) analyzed pyroxene on Mars and estimated the relative composition ratio of Opx and Cpx through the normalized band strength ratio (NBSR) of the Gaussian curve, however, due to the limitations of remote sensing with a low SNR, the accuracy decline was about 10% and it was pointed out that careful approach is needed for the analysis. Trang et al. (2013) showed the effect of impurities other than specific minerals on the MGM results

for each spectral line of Ol and pyroxene, and showed that the relationship between impurities and Fe content deforms the spectral lines.

Pl are distributed throughout the Moon, but their spectral characteristics are not prominent compared to mafic minerals. Thus, in the general observation data, the characteristics of Pl are masked by other minerals, especially when combined with Ol (Cheek & Pieters 2014). From the non-laboratory observation data, pure anorthosite regions which are rare on the Moon show the strong spectral characteristics of Pl (Otake et al. 2009).

When using the MGM technique, the most important thing is to set the initial conditions, and previous studies also made a significant effort to set the initial conditions (Sunshine et al. 1990, 1993; Sunshine & Pieters 1998; Noble et al. 2006; Denevi et al. 2007; Kanner et al. 2007; Isaacson & Pieters 2010; Isaacson et al. 2011; Trang et al. 2013; Cheek & Pieters 2014; Li et al. 2019a; Gou et al. 2020). The reason why setting proper initial conditions is important is that, due to the characteristics of decomposing spectral lines into Gaussian curves by mathematical calculation, there is a possibility that non-physical initial conditions produce results that seem to have scientific significance. The method of setting the initial conditions mainly utilizes the information of the Gaussian curve obtained by applying MGM to the spectral lines of a pure single mineral in the mineral spectroscopy list and minerals whose composition ratios are accurately known. Next, by combining the Gaussian curve information obtained from each mineral, several artificial spectral suites are created and those are set as the MGM initial conditions of the observation data. By comparing the root mean square (RMS) of each result, the mineral combination with the minimum value is interpreted as the mineral combination of observation data. In this study, the initial conditions and the mineral combination of Li et al. (2019a) are used as an example case, and initial conditions will be derived as a follow-up study. Four mineral combinations are considered in this study: Set A (Ol + Opx), Set B (Opx + Pl), Set C (Opx + Cpx + Pl), and Set D (Ol + Opx + Cpx).

Ol are decomposed into three Gaussian curves, and the composition ratio of Fe and Mg can be inferred according to the position of the central wavelength of each curve. According the central wavelength, these curves divided into M1-1 (860 nm), M2 (1,050 nm), and M1-2 (1,250 nm). As the ratio of Mg increases near each wavelength, it tends to move toward shorter wavelengths (Sunshine & Pieters 1998). Pyroxene decomposes into two Gaussian curves for both Opx and Cpx, and as the ratio of Ca increases around 1,000 nm and 2,000 nm, the wavelength center of each

curve tends to move toward longer wavelengths (Kanner et al. 2007). In order to find out the composition ratio of combined minerals, the NBSR suggested by Kanner et al. (2007) is calculated. NSBR can be calculated as follows.

$$\text{NBSR}(A) = \frac{\text{BD}(A)}{\text{BD}(A) + \text{BD}(B) + \text{BD}(C)}$$

Where, A, B, C are the minerals of combination, and BD(A) is the band depth of the Gaussian curve of the mineral A. As the number of minerals increases, the number of terms in the denominator is added. In the case of Ol, M2 can be applied while pyroxene can be applied to both Gaussian curves of 1,000 nm and 2,000 nm, but the 2,000 nm region has no information about Ol. Hence, the 2,000 nm region is not used when Ol is included in the mineral combination, and only the 1,000 nm region is used.

2.3 Targets

Identification of the distribution of Ol in the IMP areas uses the SELENE multi-band imager (MI) Ol weight percent

(wt%) map made by Lemelin et al. (2019). The spatial resolution of this map is 60 m per pixel, and the results of multi-spectral image processing have been verified by laboratory sample analysis. Although there are errors in some areas, it is useful for simply checking the distribution of minerals at a specific location throughout the Moon, and no significant error was found in the areas for this study. Since IMPs are represented by only a few pixels except for a few cases in the M3 spectroscopic image, it is difficult to identify the distribution of Ol in the IMP region. Thus, in the MI Ol map, IMPs with Ol content greater than 20wt% were selected (Table 1) and among 91 IMPs, the number of selected IMPs is 6 (Table 1).

3. RESULTS AND DISCUSSION

Parameters and figures of MGM results for 6 IMPs are shown in Tables 2–7 and Fig. 2. RMS values of the four mineral combinations show that the RMS of Set D is the lowest among all 6 IMPs (Table 8). The residual (red line) in Fig. 2 shows that the variation tends to be rather large, except for the Ina region. The reason for this is that Ina

Table 1. IMP with high olivine content

Name*	Latitude	Longitude	M3 data name
Aristarchus north	25.04°N	46.77°W	M3G20090612T060502
Unnamed 1	26.78°N	42.97°W	M3G20090208T214811
Unnamed 2	14.59°N	33.98°W	M3G20090611T043527
Unnamed 3	14.46°N	33.73°W	M3G20090611T043527
Unnamed 4	14.44°N	33.66°W	M3G20090611T043527
Ina	18.65°N	5.29°E	M3G20090205T071411

*Name is from the list of distributed IMPs. Numbers after Unnamed are assigned for identification.
IMP, irregular mare patch; M3, Moon mineralogy mapper.

Table 2. Modified Gaussian model result of Aristarchus north (Continued on the next page)

Gaussian parameters	Set A		Set B		Set C		Set D		
	Set	Fit	Set	Fit	Set	Fit	Set	Fit	
Band 1	Center	540	517.1	540	517.5	540	519.4	540	517.8
	Width	110	114.7	110	113.0	110	114.2	110	112.9
	Strength	-0.2	-0.13	-0.2	-0.13	-0.2	-0.13	-0.2	-0.13
Band 2	Center	700	651.6	700	648.5	700	653.7	700	648.2
	Width	115	123.4	115	120.6	115	123.8	115	119.7
	Strength	-0.1	-0.05	-0.1	-0.05	-0.1	-0.05	-0.1	-0.05
Band 3	Center	870	833.9	930	973.8	930	945.1	880	843.5
	Width	115	144.4	270	261.4	210	231.3	170	179.9
	Strength	-0.08	-0.05	-0.25	-0.17	-0.25	-0.13	-0.1	-0.04
Band 4	Center	915	968.1	1,300	1,265.4	980	1,056.7	915	945.1
	Width	120	169.5	260	284.7	200	236.2	178	181.5
	Strength	-0.25	-0.2	-0.02	-0.03	-0.11	-0.06	-0.25	-0.08
Band 5	Center	1,050	1,099.2	1,980	2,123.0	1,290	1,296.3	1,000	977.9
	Width	80	158.8	340	683.6	260	297.5	100	121.8
	Strength	-0.08	-0.06	-0.1	-0.1	-0.02	-0.03	-0.1	-0.03

(Table 2. Continued)

Gaussian parameters	Set A		Set B		Set C		Set D		
	Set	Fit	Set	Fit	Set	Fit	Set	Fit	
Band 6	Center	1,250	1,262.2			1,980	1,963.2	1,050	1,068.7
	Width	225	273.0			290	459.3	205	218.8
	Strength	-0.1	-0.03			-0.1	-0.09	-0.1	-0.09
Band 7	Center	1,950	2,122.8			2,250	2,334.9	1,250	1,304.0
	Width	300	687.2			160	359.8	200	229.7
	Strength	-0.1	-0.1			-0.1	-0.07	-0.1	-0.03
Band 8	Center							1,985	2,046.5
	Width							270	599.2
	Strength							-0.1	-0.09
Band 9	Center							2,215	2,395.2
	Width							160	282.6
	Strength							-0.07	-0.04
RMS error	5.273265E-003		5.495251E-003		5.703818E-003		5.067869E-003		

RMS, root mean square.

(Table 3. Modified Gaussian model result of Unnamed 1

Gaussian parameters	Set A		Set B		Set C		Set D		
	Set	Fit	Set	Fit	Set	Fit	Set	Fit	
Band 1	Center	540	531.1	540	528.2	540	526.4	540	531.4
	Width	110	118.6	110	115.4	110	114.0	110	115.0
	Strength	-0.2	-0.13	-0.2	-0.14	-0.2	-0.14	-0.2	-0.14
Band 2	Center	700	659.3	700	646.3	700	641.2	700	653.3
	Width	115	122.6	115	119.5	115	116.6	115	118.4
	Strength	-0.1	-0.05	-0.1	-0.05	-0.1	-0.05	-0.1	-0.05
Band 3	Center	870	853.5	930	988.0	930	856.1	880	844.7
	Width	115	159.6	270	325.5	210	218.7	170	180.0
	Strength	-0.08	-0.08	-0.25	-0.15	-0.25	-0.06	-0.1	-0.06
Band 4	Center	915	1,002.1	1,300	1,347.7	980	1,021.8	915	923.6
	Width	120	159.0	260	295.9	200	211.3	178	179.8
	Strength	-0.25	-0.2	-0.02	-0.04	-0.11	-0.13	-0.25	-0.05
Band 5	Center	1,050	1,119.7	1,980	2,121.3	1,290	1,289.0	1,000	1,008.0
	Width	80	154.1	340	512.7	260	320.6	100	117.6
	Strength	-0.08	-0.04	-0.1	-0.06	-0.02	-0.05	-0.1	-0.06
Band 6	Center	1,250	1,286.1			1,980	2,038.6	1,050	1,080.2
	Width	225	327.1			290	385.0	205	230.8
	Strength	-0.1	-0.05			-0.1	-0.06	-0.1	-0.09
Band 7	Center	1,950	2,120.4			2,250	2,378.0	1,250	1,332.5
	Width	300	531.9			160	254.5	200	272.9
	Strength	-0.1	-0.06			-0.1	-0.04	-0.1	-0.04
Band 8	Center							1,985	2,054.0
	Width							270	471.5
	Strength							-0.1	-0.06
Band 9	Center							2,215	2,401.5
	Width							160	245.5
	Strength							-0.07	-0.03
RMS error	7.816006E-003		8.778383E-003		8.282796E-003		7.573373E-003		

RMS, root mean square.

has a large area and is represented by several pixels in the M3 image, and while applying MGM to the spectral line corresponding to the average of the pixels, it seems that most of the noise was removed in the process of calculating the average. Since the area of the remaining IMPs cannot

be estimated, the MGM was applied to the spectral line for a single pixel, and the residual variation seems to have increased due to the noise of each spectral line. NBSR is around 1,000 nm and showed a composition in the order of Ol-Opx-Cpx as shown in Table 9.

Table 4. Modified Gaussian model result of Unnamed 2

Gaussian parameters	Set A		Set B		Set C		Set D		
	Set	Fit	Set	Fit	Set	Fit	Set	Fit	
Band 1	Center	540	554.9	540	553.5	540	556.6	540	557.5
	Width	110	138.9	110	132.0	110	133.7	110	128.7
	Strength	-0.2	-0.1	-0.2	-0.13	-0.2	-0.13	-0.2	-0.13
Band 2	Center	700	733.6	700	704.2	700	730.4	700	723.5
	Width	115	127.9	115	120.9	115	127.2	115	122.8
	Strength	-0.1	-0.04	-0.1	-0.03	-0.1	-0.04	-0.1	-0.03
Band 3	Center	870	887.6	930	1,002.2	930	980.6	880	871.6
	Width	115	148.6	270	318.0	210	243.6	170	173.0
	Strength	-0.08	-0.06	-0.25	-0.13	-0.25	-0.13	-0.1	-0.02
Band 4	Center	915	1,015.2	1,300	1,306	980	1,196.9	915	934.0
	Width	120	173.8	260	339.6	200	247.4	178	184.9
	Strength	-0.25	-0.1	-0.02	-0.03	-0.11	-0.06	-0.25	-0.08
Band 5	Center	1,050	1,183.8	1,980	2,104.4	1,290	1,465.8	1,000	1,020.9
	Width	80	187.7	340	787.5	260	327.3	100	115.4
	Strength	-0.08	-0.06	-0.1	-0.12	-0.02	-0.03	-0.1	-0.05
Band 6	Center	1,250	1,363.0			1,980	1,945.0	1,050	1,140.9
	Width	225	317.3			290	480.6	205	231.9
	Strength	-0.1	-0.03			-0.1	-0.1	-0.1	-0.08
Band 7	Center	1,950	2,105.1			2,250	2,350.0	1,250	1,370.9
	Width	300	781.9			160	390.0	200	253.3
	Strength	-0.1	-0.1			-0.1	-0.09	-0.1	-0.03
Band 8	Center							1,985	2,023.6
	Width							270	684.1
	Strength							-0.1	-0.1
Band 9	Center							2,215	2,414.0
	Width							160	296.8
	Strength							-0.07	-0.04
RMS error	6.909274E-003		7.366668E-003		6.963749E-003		6.656025E-003		

RMS, root mean square.

Table 5. Modified Gaussian model result of Unnamed 3 (Continued on the next page)

Gaussian parameters	Set A		Set B		Set C		Set D		
	Set	Fit	Set	Fit	Set	Fit	Set	Fit	
Band 1	Center	540	567.9	540	564.0	540	567.5	540	567.0
	Width	110	122.1	110	116.0	110	118.3	110	115.8
	Strength	-0.2	-0.1	-0.2	-0.1	-0.2	-0.1	-0.2	-0.1
Band 2	Center	700	711.5	700	681.5	700	703.1	700	699.0
	Width	115	119.8	115	115.3	115	119.0	115	117.2
	Strength	-0.1	-0.04	-0.1	-0.03	-0.1	-0.03	-0.1	-0.04
Band 3	Center	870	859.4	930	968.9	930	944.4	880	880.0
	Width	115	114.5	270	293.4	210	215.4	170	169.5
	Strength	-0.08	-0.05	-0.25	-0.09	-0.25	-0.1	-0.1	-0.03
Band 4	Center	915	965.9	1,300	1,226.0	980	1,147.8	915	913.3
	Width	120	126.7	260	305.7	200	227.2	178	177.6
	Strength	-0.25	-0.09	-0.02	-0.04	-0.11	-0.06	-0.25	-0.04
Band 5	Center	1,050	1,094.0	1,980	2,118.1	1,290	1,386.3	1,000	975.3
	Width	80	136.5	340	749.0	260	313.0	100	90.8
	Strength	-0.08	-0.05	-0.1	-0.1	-0.02	-0.02	-0.1	-0.03
Band 6	Center	1,250	1,217.0			1,980	1,975.1	1,050	1,100.3
	Width	225	287.8			290	481.9	205	217.5
	Strength	-0.1	-0.05			-0.1	-0.1	-0.1	-0.08
Band 7	Center	1,950	2,117.3			2,250	2,381.3	1,250	1,306.9
	Width	300	756.7			160	333.0	200	217.5
	Strength	-0.1	-0.1			-0.1	-0.07	-0.1	-0.08

(Table 5. Continued)

Gaussian parameters	Set A		Set B		Set C		Set D	
	Set	Fit	Set	Fit	Set	Fit	Set	Fit
Band 8	Center						1,985	2,023.8
	Width						270	628.8
	Strength						-0.1	-0.09
Band 9	Center						2,215	2,417.7
	Width						160	267.8
	Strength						-0.07	-0.04
RMS error	7.085348E-003		7.697302E-003		7.335101E-003		6.715334E-003	

RMS, root mean square.

Table 6. Modified Gaussian model result of Unnamed 4

Gaussian parameters	Set A		Set B		Set C		Set D		
	Set	Fit	Set	Fit	Set	Fit	Set	Fit	
Band 1	Center	540	561.0	540	553.7	540	560.8	540	560.3
	Width	110	140.0	110	132.0	110	135.6	110	128.6
	Strength	-0.2	-0.1	-0.2	-0.1	-0.2	-0.1	-0.2	-0.1
Band 2	Center	700	703.7	700	673.8	700	697.4	700	689.7
	Width	115	130.8	115	127.9	115	131.3	115	125.7
	Strength	-0.1	-0.06	-0.1	-0.05	-0.1	-0.05	-0.1	-0.06
Band 3	Center	870	865.5	930	982.0	930	941.1	880	842.0
	Width	115	157.9	270	373.0	210	266.8	170	181.2
	Strength	-0.08	-0.08	-0.25	-0.1	-0.25	-0.1	-0.1	-0.05
Band 4	Center	915	998.8	1,300	1,297.4	980	1,159.2	915	939.9
	Width	120	165.2	260	352.9	200	272.9	178	181.2
	Strength	-0.25	-0.1	-0.02	-0.04	-0.11	-0.07	-0.25	-0.07
Band 5	Center	1,050	1,131.2	1,980	2,114.0	1,290	1,432.0	1,000	1,015.5
	Width	80	168.7	340	757.4	260	348.8	100	112.0
	Strength	-0.08	-0.05	-0.1	-0.1	-0.02	-0.03	-0.1	-0.03
Band 6	Center	1,250	1,257.8			1,980	1,973.4	1,050	1,115.6
	Width	225	327.8			290	495.1	205	231.8
	Strength	-0.1	-0.05			-0.1	-0.1	-0.1	-0.09
Band 7	Center	1,950	2,111.5			2,250	2,368.8	1,250	1,324.3
	Width	300	774.2			160	354.4	200	260.4
	Strength	-0.1	-0.1			-0.1	-0.08	-0.1	-0.04
Band 8	Center							1,985	2,026.4
	Width							270	675.6
	Strength							-0.1	-0.1
Band 9	Center							2,215	2,399.4
	Width							160	273.5
	Strength							-0.07	-0.05
RMS error	8.609963E-003		8.734551E-003		8.567078E-003		8.414062E-003		

RMS, root mean square.

Table 7. Modified Gaussian model result of Ina (Continued on the next page)

Gaussian parameters	Set A		Set B		Set C		Set D		
	Set	Fit	Set	Fit	Set	Fit	Set	Fit	
Band 1	Center	540	530.0	540	532.9	540	530.5	540	830.6
	Width	110	120.8	110	122.5	110	116.5	110	116.4
	Strength	-0.2	-0.1	-0.2	-0.1	-0.2	-0.1	-0.2	-0.1
Band 2	Center	700	670.3	700	678.7	700	661.4	700	661.1
	Width	115	139.6	115	148.2	115	130.1	115	129.4
	Strength	-0.1	-0.08	-0.1	-0.08	-0.1	-0.07	-0.1	-0.08
Band 3	Center	870	857.7	930	993.0	930	831.6	880	807.6
	Width	115	177.4	270	270.0	210	232.9	170	186.5
	Strength	-0.08	-0.05	-0.25	-0.1	-0.25	-0.04	-0.1	-0.04

(Table 7. Continued)

Gaussian parameters	Set A		Set B		Set C		Set D		
	Set	Fit	Set	Fit	Set	Fit	Set	Fit	
Band 4	Center	915	1,021.0	1,300	1,567.2	980	1,018.7	915	955.9
	Width	120	192.8	260	434.1	200	220.1	178	176.1
	Strength	-0.25	-0.1	-0.02	-0.05	-0.11	-0.12	-0.25	-0.07
Band 5	Center	1,050	1,231.2	1,980	2,233.0	1,290	1,529.9	1,000	1,041.2
	Width	80	181.8	340	619.2	260	396.3	100	116.7
	Strength	-0.08	-0.01	-0.1	-0.09	-0.02	-0.05	-0.1	-0.04
Band 6	Center	1,250	1,572.0			1,980	2,021.0	1,050	1,071.7
	Width	225	435.6			290	419.8	205	234.5
	Strength	-0.1	-0.05			-0.1	-0.07	-0.1	-0.06
Band 7	Center	1,950	2,234.7			2,250	2,374.3	1,250	1,493.5
	Width	300	627.1			160	344.1	200	319.8
	Strength	-0.1	-0.1			-0.1	-0.08	-0.1	-0.04
Band 8	Center							1,985	2,054.5
	Width							270	602.4
	Strength							-0.1	-0.07
Band 9	Center							2,215	2,398.1
	Width							160	312.0
	Strength							-0.07	-0.05
RMS error	3.837276E-003		5.184219E-003		3.909666E-003		3.762563E-003		

RMS, root mean square.

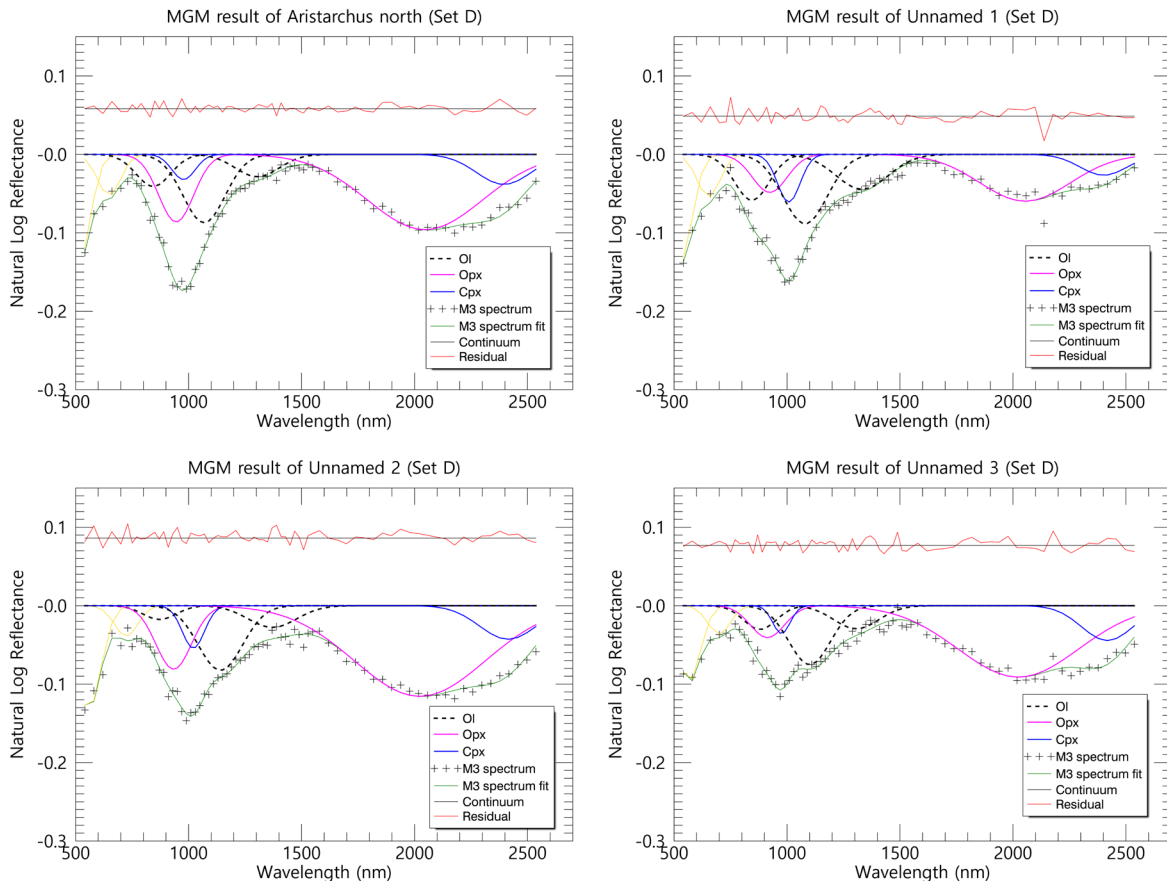
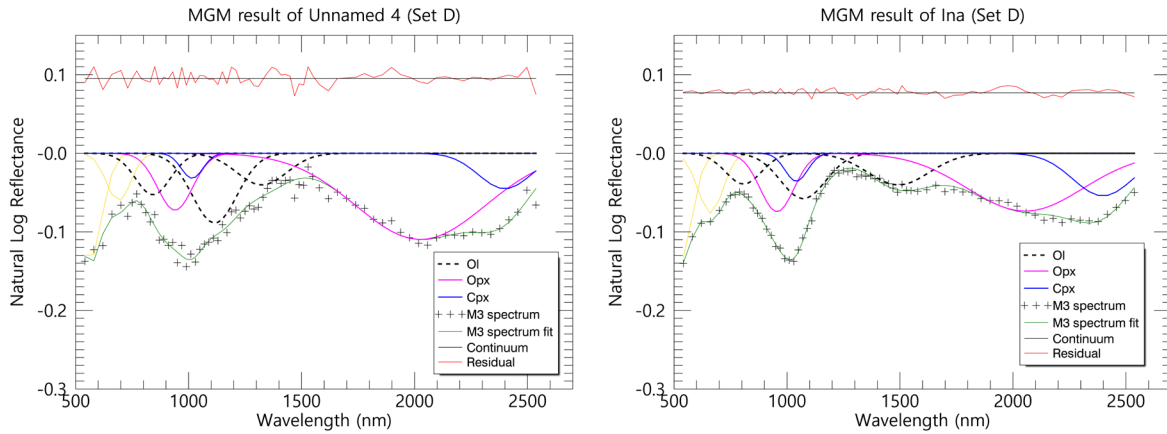


Fig. 2. MGM results for Set D. It can be seen that the observed data (cross symbol '+') and the combination of the Gaussian curves (green solid line) agrees. OI are represented by a black dotted line, Opx by a magenta solid line, and Cpx by a blue solid line. MGM, modified Gaussian model; OI, olivine; Opx, orthopyroxene; Cpx, clinopyroxene; M3, Moon mineralogy mapper. (Continued on the next page.)

(Fig. 2. Continued)

**Table 8.** RMS error of modified Gaussian model results for each set in the IMP regions

Name*	Latitude	Longitude	M3 data name	RMS error			
				Set A	Set B	Set C	Set D
Aristarchus north	25.04°N	46.77°W	M3G20090612T060502	3.86×10^{-3}	4.13×10^{-3}	3.75×10^{-3}	2.99×10^{-3}
Unnamed 1	26.78°N	42.97°W	M3G20090208T214811	3.20×10^{-3}	3.29×10^{-3}	2.99×10^{-3}	2.34×10^{-3}
Unnamed 2	14.59°N	33.98°W	M3G20090611T043527	2.72×10^{-3}	3.05×10^{-3}	3.16×10^{-3}	2.00×10^{-3}
Unnamed 3	14.46°N	33.73°W	M3G20090611T043527	2.59×10^{-3}	2.76×10^{-3}	2.87×10^{-3}	2.00×10^{-3}
Unnamed 4	14.44°N	33.66°W	M3G20090611T043527	2.61×10^{-3}	2.80×10^{-3}	2.90×10^{-3}	2.07×10^{-3}
Ina	18.65°N	5.29°E	M3G20090205T071411	3.00×10^{-3}	3.53×10^{-3}	3.12×10^{-3}	2.29×10^{-3}

*Name is from the list of distributed IMPs. Numbers after Unnamed are assigned for identification.

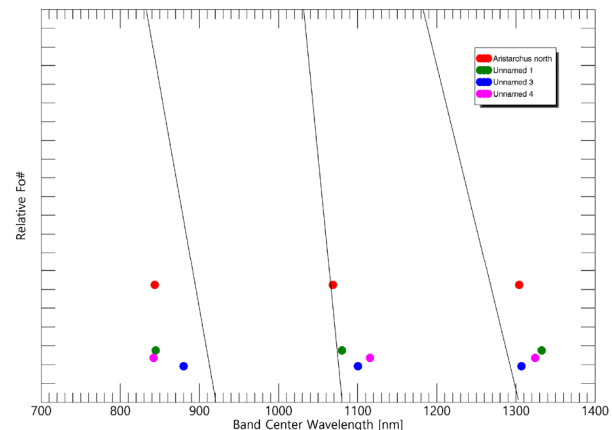
RMS, root mean square; IMP, irregular mare patch; M3, Moon mineralogy mapper.

Table 9. Set D NBSR of irregular mare patches

Name	NBSR (OI)	NBSR (Opx)	NBSR (Cpx)
Aristarchus north	0.42	0.42	0.17
Unnamed 1	0.45	0.25	0.31
Unnamed 2	0.34	0.442	0.21
Unnamed 3	0.50	0.27	0.23
Unnamed 4	0.38	0.377	0.25
Ina	0.46	0.38	0.17

NBSR, normalized band strength ratio; OI, olivine; Opx, orthopyroxene; Cpx, clinopyroxene.

The Ol Gaussian curves, M1-1, M2, and M1-2 are shown in Fig. 3. We could get the results for only 4 out of 6 IMPs. The two produced values out of the Y-axis range of the figure and it is suspected that an error was introduced when applying MGM. One of the possible causes for this error is the noise of the spectral line resulting in the inaccurate calculation. Also, a problem in setting the initial conditions could contribute to this error. Noise in observation data is a problem caused by using a spectral line of a single pixel. And the solution for this is to utilize high-resolution optical images to enable a selection of several pixels constituting IMP, thus, it is necessary to supplement the data collection stage. The problem of setting the initial conditions can be

**Fig. 3.** Band position of olivine Gaussian curve in the irregular mare patch regions. Only 4 out of 6 areas showed significant results, and all of them show a low Fo# (high Fa) content ratio, so it can be said that there is little relationship with Mg-suite rock. The other two are not shown in the figure because relative Fo# is beyond the y-axis range due to a problem in the process of applying modified Gaussian model.

regarded as a fundamental limitation of this study. The initial conditions derived in other studies are used for this study instead of deriving the MGM initial condition

values by finding samples similar to the spectral lines of the observation data with the data in the spectral library. Thus, the results seem scientifically meaningful, but it is a weak justification. It is necessary to determine the proper initial conditions consistent with the observation data through follow-up studies on this issue. All of the Ol characteristics of the four regions where the results were obtained showed a very high content of fayalite, which suggests that these regions are not related to Mg-suite magma.

The lunar rock formation is different from that of the Earth and is characterized by the low partial pressure of oxygen. The low oxygen partial pressure prevents the formation of Fe³⁺ in the magma, so minerals mainly Fe²⁺ crystallize, and oxide minerals such as FeO and silicate minerals including fayalite are produced (Heiken et al. 1991). Most lunar oxygen is contained in silicate minerals, which are more abundant than oxide minerals. Therefore, pyroxene with a lot of Fe is evenly distributed throughout the mafic mare. Olivine, which has a relatively low composition ratio compared to pyroxene, exists mainly in fayalite, and Mg-suite rocks are rare.

4. CONCLUSION

In order to find out the Ol characteristics of the magma eruption area of IMPs which are believed to be created relatively recently, the MGM technique was applied to determine which element was more abundant in the area, Fe or Mg. Since the age of the areas of study is rather young and the time exposed to the space environment is small, it was expected that the deformation of the spectral lines would be less, and it would be possible to determine the clear characteristics of Ol. However, the age of IMPs may be older depending on the hypothesis of IMP formation. In the MGM results, the Ol-rich IMP regions are predominantly abundant in fayalite and showed little relationship with Mg-suite magma.

Through the results of this study, we identified the compositional characteristics of the regions which have not yet been attempted in other studies, for the first time. However, it is necessary to take into account the decrease in reliability due to noise in the observation data and problems found in the initial condition setting of the MGM. On second thought, it can be said that the foundation for enhancing the degree of completion in the follow-up study was established because issues were clearly identified. Also, through further study, it is necessary to classify the mineral properties of all IMPs discovered so far, not limited to mafic minerals, in order to utilize them to infer the origin of each IMP.

ACKNOWLEDGMENTS

This research was supported by the National Research Foundation of Korea (NRF) grant funded by the Korea government (MSIT) (NRF-2022R1A2C1092602).

ORCIDs

Ik-Seon Hong	https://orcid.org/0000-0002-4529-8002
Yu Yi	https://orcid.org/0000-0001-9348-454X
Nuri Park	https://orcid.org/0000-0002-3153-0157

REFERENCES

- Basaltic Volcanism Study Project (BVSP), Basaltic Volcanism on the Terrestrial Planets (Pergamon Press, Inc., New York, 1981).
- Bibring JP, Langevin Y, Mustard JF, Poulet F, Arvidson R, Global mineralogical and aqueous mars history derived from OMEGA/Mars Express data, *Science* 312, 400-404 (2006). <https://doi.org/10.1126/science.1122659>
- Braden SE, Stopar JD, Robinson MS, Lawrence SJ, Van Der Bogert CH, et al., Evidence for basaltic volcanism on the Moon within the past 100 million years, *Nat. Geosci.* 7, 787-791 (2014). <https://doi.org/10.1038/ngeo2252>
- Byron BD, Elder CM, Williams JP, Ghent RR, Gallinger CL, et al., Thermophysical properties of lunar irregular mare patches from LRO diviner radiometer data, *J. Geophys. Res. Planets* 127, e2022JE007214 (2022). <https://doi.org/10.1029/2022JE007214>
- Charlier B, Grove TL, Namur O, Holtz F, Crystallization of the lunar magma ocean and the primordial mantle-crust differentiation of the Moon, *Geochim. Cosmochim. Acta* 234, 50-69 (2018). <https://doi.org/10.1016/j.gca.2018.05.006>
- Cheek LC, Pieters CM, The Second Conference on the Lunar Highlands Crust and New Directions. Reflectance spectroscopy of plagioclase-dominated mineral mixtures: Implications for characterizing lunar anorthosites remotely, *Am. Mineral.* 99, 1871-1892 (2014). <https://doi.org/10.2138/am-2014-4785>
- Chen J, Ling Z, Qiao L, He Z, Xu R, Mineralogy of Chang'e-4 landing site: preliminary results of visible and near-infrared imaging spectrometer, *Sci. China Inf. Sci.* 63, 140903 (2020). <https://doi.org/10.1007/s11432-019-2768-1>
- Clark RN, Pieters CM, Green RO, Boardman JW, Petro NE, Thermal removal from near-infrared imaging spectroscopy data of the Moon, *J. Geophys. Res.* 116, E00G16 (2011). <https://doi.org/10.1029/2010JE003751>

- Cushing GE, Candidate cave entrances on Mars, *J. Cave Karst Stud.* 74, 33-47 (2012). <https://doi.org/10.4311/2010EX0167R>
- Cushing GE, Titus TN, Wynne JJ, Christensen PR, THEMIS observes possible cave skylights on Mars, *Geophys. Res. Lett.* 34, L17201 (2007). [http://doi.org/10.1029/2007GL030709](https://doi.org/10.1029/2007GL030709)
- Denevi BW, Lucey PG, Hochberg EJ, Steutel D, Near-infrared optical constants of pyroxene as a function of iron and calcium content, *J. Geophys. Res.* 112, E05009 (2007). <https://doi.org/10.1029/2006JE002802>
- Elardo SM, Draper DS, Shearer CK Jr, Lunar magma ocean crystallization revisited: bulk composition, early cumulate mineralogy, and the source regions of the highlands Mg-suite, *Geochim. Cosmochim. Acta* 75, 3024-3045 (2011). <https://doi.org/10.1016/j.gca.2011.02.033>
- Garry WB, Robinson MS, Zimbelman JR, Bleacher JE, Hawke BR, et al., The origin of Ina: evidence for inflated lava flows on the Moon, *J. Geophys. Res.* 117, E00H31 (2012). <https://doi.org/10.1029/2011JE003981>
- Gou S, Di K, Yue Z, Liu Z, He Z, et al., Forsteritic olivine and magnesium-rich orthopyroxene materials measured by Chang'e-4 rover, *Icarus* 345, 113776 (2020). <https://doi.org/10.1016/j.icarus.2020.113776>
- Green RO, Pieters C, Mouroulis P, Eastwood M, Boardman J, et al., The moon mineralogy mapper (M^3) imaging spectrometer for lunar science: instrument description, calibration, on-orbit measurements, science data calibration and on-orbit validation, *J. Geophys. Res.* 116, E00G19 (2011). <https://doi.org/10.1029/2011JE003797>
- Grier JA, McEwen AS, Lucey PG, Milazzo M, Strom RG, Optical maturity of ejecta from large rayed lunar craters, *J. Geophys. Res.* 106, 32847-32862 (2001). <https://doi.org/10.1029/1999JE001160>
- Heiken GH, Vaniman DT, French BM, *Lunar Sourcebook* (Cambridge University Press, Cambridge, 1991).
- Hess PC, Parmentier EM, A model for the thermal and chemical evolution of the Moon's interior: implications for the onset of mare volcanism, *Earth Planet. Sci. Lett.* 134, 501-514 (1995). [https://doi.org/10.1016/0012-821X\(95\)00138-3](https://doi.org/10.1016/0012-821X(95)00138-3)
- Hong IS, Yi Y, Kim E, Lunar pit craters presumed to be the entrances of lava caves by analogy to the earth lava tube pits, *J. Astron. Space Sci.* 31, 131-140 (2014). <http://doi.org/10.5140/JASS.2014.31.2.131>
- Isaacson PJ, Petro NE, Pieters CM, Besse S, Boardman JW, et al., Development, importance, and effect of a ground truth correction for the Moon mineralogy mapper reflectance data set, *J. Geophys. Res. Planets* 118, 369-381 (2013). <https://doi.org/10.1002/jgre.20048>
- Isaacson PJ, Pieters CM, Deconvolution of lunar olivine reflectance spectra: implications for remote compositional assessment, *Icarus* 210, 8-13 (2010). <https://doi.org/10.1016/j.icarus.2010.06.004>
- Isaacson PJ, Pieters CM, Besse S, Clark RN, Head JW, et al., Remote compositional analysis of lunar olivine-rich lithologies with Moon mineralogy mapper (M^3) spectra, *J. Geophys. Res.* 116, E00G11 (2011). <https://doi.org/10.1029/2010JE003731>
- Jung J, Hong IS, Cho E, Yi Y, Method for identifying lava tubes among pit craters using brightness profile across pits on the Moon or mars, *J. Astron. Space Sci.* 33, 21-28 (2016). <https://doi.org/10.5140/JASS.2016.33.1.21>
- Jung J, Yi Y, Kim E, Identification of martian cave skylights using the temperature change during day and night, *J. Astron. Space Sci.* 31, 141-144 (2014). <https://doi.org/10.5140/JASS.2014.31.2.141>
- Kanner LC, Mustard JF, Gendrin A, Assessing the limits of the modified Gaussian model for remote spectroscopic studies of pyroxenes on Mars, *Icarus* 187, 442-456 (2007). <https://doi.org/10.1016/j.icarus.2006.10.025>
- Kim SY, Yi Y, Hong IS, Sohn J, Solar insolation effect on the local distribution of lunar hydroxyl, *J. Astron. Space Sci.* 35, 47-54 (2018). <https://doi.org/10.5140/JASS.2018.35.1.47>
- King TVV, Ridley WI, Relation of the spectroscopic reflectance of olivine to mineral chemistry and some remote sensing implications, *J. Geophys. Res.* 92, 11457-11469 (1987). <https://doi.org/10.1029/JB092iB11p11457>
- Lemelin M, Lucey PG, Miljković K, Gaddis LR, Hare T, The compositions of the lunar crust and upper mantle: spectral analysis of the inner rings of lunar impact basins, *Planet. Space Sci.* 165, 230-243 (2019). <https://doi.org/10.1016/j.pss.2018.10.003>
- Li C, Liu D, Liu B, Ren X, Liu J, et al., Chang'E-4 initial spectroscopic identification of lunar far-side mantle-derived materials, *Nature* 569, 378-382 (2019a). <https://doi.org/10.1038/s41586-019-1189-0>
- Li H, Zhang N, Liang Y, Wu B, Dygert NJ, et al., Lunar cumulate mantle overturn: a model constrained by ilmenite rheology, *J. Geophys. Res. Planets* 124, 1357-1378 (2019b). <https://doi.org/10.1029/2018JE005905>
- Li S, Milliken RE, An empirical thermal correction model for Moon mineralogy mapper data constrained by laboratory spectra and diviner temperatures, *J. Geophys. Res. Planets* 121, 2081-2107 (2016). <https://doi.org/10.1002/2016JE005035>
- Lucey PG, Blewett DT, Taylor GJ, Hawke BR, Imaging of lunar surface maturity, *J. Geophys. Res.* 105, 20377-20386 (2000). <https://doi.org/10.1029/1999JE001110>
- Lucey PG, Taylor GJ, Malaret E, Abundance and distribution of iron on the Moon, *Science* 268, 1150-1153 (1995). <https://doi.org/10.1126/science.268.5214.1150>
- McCord TB, Adams JB, Progress in remote optical analysis of lunar surface composition, *Moon* 7, 453-474 (1973). <https://doi.org/10.1016/j.moon.1973.01.003>

- doi.org/10.1007/BF00564646
- McCord TB, Johnson TV, Lunar spectral reflectivity (0.30 to 2.50 microns) and implications for remote mineralogical analysis, *Science* 169, 855-858 (1970). <https://doi.org/10.1126/science.169.3948.855>
- McEwen AS, Robinson MS, Mapping of the Moon by Clementine. *Adv. Space Res.* 19, 1523-1533 (1997). [https://doi.org/10.1016/S0273-1177\(97\)00365-7](https://doi.org/10.1016/S0273-1177(97)00365-7)
- Melosh HJ, Kendall J, Horgan B, Johnson BC, Bowling T, et al., South pole-Aitken basin ejecta reveal the Moon's upper mantle, *Geology* 45, 1063-1066 (2017). <https://doi.org/10.1130/G39375.1>
- Noble SK, Pieters CM, Hiroi T, Taylor LA, Using the modified Gaussian model to extract quantitative data from lunar soils, *J. Geophys. Res.* 111, E11009 (2006). <https://doi.org/10.1029/2006JE002721>
- Nozette S, Rustan P, Pleasance LP, Kordas JF, Lewis IT, et al., The Clementine mission to the Moon: scientific overview, *Science* 266, 1835-1839 (1994). <https://www.doi.org/10.1126/science.266.5192.1835>
- Ohtake M, Haruyama J, Matsunaga T, Yokota Y, Morota T, et al., Performance and scientific objectives of the SELENE (Kaguya) multiband imager, *Earth Planets Space* 60, 257-264 (2008). <https://doi.org/10.1186/BF03352789>
- Ohtake M, Matsunaga T, Haruyama J, Yokota Y, Morota T, et al., The global distribution of pure anorthosite on the Moon, *Nature* 461, 236-240 (2009). <https://doi.org/10.1038/nature08317>
- Pelkey SM, Mustard JF, Murchie S, Clancy RT, Wolff M, et al., CRISM multispectral summary products: parameterizing mineral diversity on Mars from reflectance, *J. Geophys. Res.* 112, E08S14 (2007). <https://doi.org/10.1029/2006JE002831>
- Pieters CM, Fischer EM, Rode O, Basu A, Optical effects of space weathering: the role of the finest fraction, *J. Geophys. Res.* 98, 20817-20824 (1993). <https://doi.org/10.1029/93JE02467>
- Pieters CM, Noble SK, Space weathering on airless bodies, *J. Geophys. Res. Planets* 121, 1865-1884 (2016). <https://doi.org/10.1002/2016JE005128>
- Pieters CM, Taylor LA, Noble SK, Keller LP, Hapke B, Space weathering on airless bodies: resolving a mystery with lunar samples, *Meteorit. Planet. Sci.* 35, 1101-1107 (2000). <https://doi.org/10.1111/j.1945-5100.2000.tb01496.x>
- Qiao L, Head JW, Ling Z, Wilson L, Lunar Irregular mare patches: classification, characteristics, geologic settings, updated catalog, origin, and outstanding questions, *J. Geophys. Res. Planets* 125, e2019JE006362 (2020). <https://doi.org/10.1029/2019JE006362>
- Ringwood AE, Kesson SE, A dynamic model for mare basalt petrogenesis, *Proceedings of the 7th Lunar Science Conference*, Houston, TX, 15-19 Mar 1976.
- Sim CK, Kim SS, Spectral trends of the surface regolith in lunar craters, *J. Geophys. Res. Planets* 123, 2065-2075 (2018). <https://doi.org/10.1029/2018JE005670>
- Sim CK, Kim SS, Lucey PG, Garrik-Bethell I, Choi YJ, Asymmetric space weathering on lunar crater walls, *Geophys. Res. Lett.* 44, 11273-11281 (2017). <https://doi.org/10.1002/2017GL075338>
- Strain PL, El-Baz F, The geology and morphology of Ina, *Proceedings of the 11th Lunar and Planetary Science Conference*, Houston, TX, 17-21 Mar 1980.
- Sunshine JM, McFadden LA, Pieters CM, Reflectance spectra of the Elephant Moraine A79001 meteorite: implications for remote sensing of planetary bodies, *Icarus* 105, 79-91 (1993). <https://doi.org/10.1006/icar.1993.1112>
- Sunshine JM, Pieters CM, Estimating modal abundances from the spectra of natural and laboratory pyroxene mixtures using the modified Gaussian model, *J. Geophys. Res.* 98, 9075-9087 (1993). <https://doi.org/10.1029/93JE00677>
- Sunshine JM, Pieters CM, Determining the composition of olivine from reflectance spectroscopy, *J. Geophys. Res.* 103, 13675-13688 (1998). <https://doi.org/10.1029/98JE01217>
- Sunshine JM, Pieters CM, Pratt SF, Deconvolution of mineral absorption bands: an improved approach, *J. Geophys. Res.* 95, 6955-6966 (1990). <https://doi.org/10.1029/JB095iB05p06955>
- Trang D, Lucey PG, Gillis-Davis JJ, Cahill JTS, Klima RL, et al., Near-infrared optical constants of naturally occurring olivine and synthetic pyroxene as a function of mineral composition, *J. Geophys. Res. Planets* 118, 708-732 (2013). <https://doi.org/10.1002/jgre.20072>
- Whitaker EA, An unusual mare feature, *Apollo 15 Preliminary Science Report*, ed. NASA (NASA, Washington, 1972).
- Wieczorek MA, Jolliff BL, Khan A, Pritchard ME, Weiss BP, et al., The constitution and structure of the Lunar interior, *Rev. Mineral. Geochem.* 60, 221-364 (2006). <https://doi.org/10.2138/rmg.2006.60.3>
- Wilson L, Head JW, Eruption of magmatic foams on the moon: formation in the waning stages of dike emplacement events as an explanation of "irregular mare patches," *J. Volcanol. Geotherm. Res.* 335, 113-127 (2017). <https://doi.org/10.1016/j.jvolgeores.2017.02.009>
- Yamamoto S, Nakamura R, Matsunaga T, Ogawa Y, Ishihara Y, et al., Possible mantle origin of olivine around lunar impact basins detected by SELENE, *Nat. Geosci.* 3, 533-536 (2010). <https://doi.org/10.1038/ngeo897>
- Yi ES, Kim KJ, Choi YR, Kim YH, Lee SS et al., Investigation of reflectance distribution and trend for the double ray located in the northwest of Tycho crater, *J. Astron. Space Sci.* 32, 161-166 (2015). <https://doi.org/10.5140/JASS.2015.32.2.161>